

Gamma-Ray Bursts: Evidence for a Common Origin of X-ray Plateaus with Diverse Temporal Decay Index

XIAO-FEI DONG ,¹ YONG-FENG HUANG ,^{1,2} CHEN DENG ,^{1,2} ZE-CHENG ZOU ,¹ JIN-JUN GENG ,³ FAN XU ,⁴ CHEN-RAN HU ,¹ ORKASH AMAT ,¹ XIU-JUAN LI ,⁵ LIANG LI ,^{6,7} AND ABDUSATTAR KURBAN ,^{8,9}

¹ School of Astronomy and Space Science, Nanjing University, Nanjing 210023, People's Republic of China

² Key Laboratory of Modern Astronomy and Astrophysics (Nanjing University), Ministry of Education, People's Republic of China

³ Purple Mountain Observatory, Chinese Academy of Sciences, Nanjing 210023, People's Republic of China

⁴ Institute of Space Weather, Nanjing University of Information Science and Technology, Nanjing 210023, People's Republic of China

⁵ School of Cyber Science and Engineering, Qufu Normal University, Qufu 273165, People's Republic of China

⁶ Institute of Fundamental Physics and Quantum Technology, Ningbo University, Ningbo, Zhejiang 315211, People's Republic of China

⁷ School of Physical Science and Technology, Ningbo University, Ningbo, Zhejiang 315211, People's Republic of China

⁸ State Key Laboratory of Radio Astronomy and Technology, Xinjiang Astronomical Observatory, CAS, 150 Science 1-Street, Urumqi, Xinjiang, 830011, People's Republic of China

⁹ Xinjiang Key Laboratory of Radio Astrophysics, Urumqi, Xinjiang, 830011, People's Republic of China

ABSTRACT

A significant fraction of gamma-ray bursts (GRBs) exhibit a plateau in the early X-ray afterglow light curve, whose mechanism remains uncertain. While the post-plateau normal decay index (α_2) is commonly used to constrain the afterglow dynamics, the shallow-decay slope of the plateau itself (α_1) has received comparatively little attention. Recent observations, however, reveal substantial dispersion in α_1 , raising the question of whether GRBs with rising, flat and mildly decaying plateaus represent intrinsically distinct populations. To address this question, we collect a uniform sample of 185 *Swift* GRBs with a well-defined plateau and divide them into three groups based on α_1 . Using a non-parametric approach, we reconstruct their X-ray luminosity functions, redshift distributions and event rates. It is found that the three groups exhibit statistically consistent properties across all diagnostics, with no evidence for group-specific features. Monte Carlo perturbation tests further show that these results are insensitive to the adopted classification boundaries of α_1 . Our results indicate that variations in the plateau slope α_1 do not define distinct GRB subclasses, but instead the sample constitutes a statistically uniform population governed by a common framework.

Keywords: Gamma-ray bursts (629); Magnetars (992); Neutron stars (1108); Monte Carlo methods (2238)

1. INTRODUCTION

The early X-ray afterglow of gamma-ray bursts (GRBs) is commonly characterized by a canonical broken power-law temporal evolution, comprising an initial steep decay, a shallow-decay (plateau), and a subsequent normal decay (Gehrels et al. 2006; Zhang et al. 2006). It is interesting to note that Du et al. (2024) recently analyzed 310 GRB X-ray afterglows and divided them into four temporal categories based on the presence of flares, plateaus, and breaks. While the steep decay is generally attributed to high-latitude emission of the prompt phase (Zhang et al. 2007; Yin et al. 2025) and the normal decay phase is broadly consistent with the predictions of the standard external forward-shock afterglow model (Sari et al. 1998; Huang et al. 1999), the plateau phase – characterized by an unusually shallow temporal evolution over a timescale of $\sim 10^{2.5} - 10^4$ s – remains to be an enigmatic component of the early afterglow (Granot & Kumar 2006; Liang et al. 2007).

Owing to their well-defined temporal and luminosity properties, X-ray plateaus provide a powerful diagnostic of the early afterglow phase. They have been widely exploited to establish a number of empirical correlations with potential cosmological applications (Dainotti et al. 2008, 2010; Xu & Huang 2012; Tang et al. 2019; Xu et al. 2021; Deng et al. 2023), to probe the features of external shock emission and the circum-burst environment (Liang et al. 2007; Shen & Matzner 2012; Tian et al. 2022), and to constrain long-lived central engine activities (Rowlinson et al. 2014; Lü et al. 2015; Li et al. 2018).

The formation mechanism of the plateau remains a long-standing question. Numerous models have been proposed, including continuous energy injection from the central engine (e.g., a spinning magnetar or a black hole undergoing fallback accretion) into the blast wave (Fan & Piran 2006; Ghisellini et al. 2007; Stratta et al. 2018; Deng et al. 2025); structured or off-axis jets (Lazzati et al. 2018; Ascenzi et al. 2020; Dereli-Bégué et al. 2022); density stratification in the circum-burst medium (Toma et al. 2006; Jin et al. 2007; Zhao 2025); reverse shock emission (Genet et al. 2007; Uhm & Beloborodov 2007; Hascoët et al. 2014; Fraija et al. 2025); scattering echoes of dust (Shao et al. 2008); and sub-relativistic cocoon or shock-breakout scenarios (Fraija et al. 2022). In addition, an apparent plateau may sometimes arise from an inappropriate choice of the reference time (Guidorzi et al. 2025).

Given the diverse theoretical possibilities, it was naturally expected that variations in the shallow-decay slope might reflect different origins. For example, in the energy-injection scenarios, sustained or effectively increasing power from a newborn millisecond magnetar can produce a flat or rising plateau (Dai & Lu 1998; Zhang & Mészáros 2001), whereas the declining fallback accretion onto a nascent black hole may result in a mildly decaying plateau (Yu et al. 2015b; Metzger et al. 2018). By contrast, structured jets and viewing-angle effects can produce diverse plateau morphology without requiring special central-engine evolution (Rossi et al. 2002; Granot & Kumar 2003; Beniamini et al. 2020).

However, different scenarios can produce similar plateau slopes, leading to significant degeneracy in the observed light curves. Consequently, many authors have relied on the post-plateau decay to infer or constrain the plateau origin, rather than directly exploiting the plateau slope itself. A normal post-plateau decay index of order unity is generally consistent with external-shock energy injection (Willingale et al. 2007), whereas an extremely steep decay ($\lesssim -3$) is commonly interpreted as an “internal plateau” connected to abruptly terminated central-engine activities (Troja et al. 2007; Lyons et al. 2010; Chen et al. 2017; Beniamini & Mochkovitch 2017).

Recent analyses have shown that the shallow-decay index displays non-negligible dispersion among different bursts (Tang et al. 2019; Deng et al. 2023; Ronchini et al. 2023; Guglielmi et al. 2024), suggesting potential diversities in the underlying mechanisms. Here we conduct a systematic population-level study to test whether the distribution of the shallow-decay index provides additional constraints on the origin of the X-ray plateau.

The paper is organized as follows. Section 2 describes the data set, subsample classification, and parameter calculations. Section 3 outlines the non-parametric methods used to derive the intrinsic luminosity function and event rate. The results for each subsample are presented in Section 4. In Section 5, we further assess the robustness of our results via Monte Carlo simulations. Section 6 summarizes the main findings, and Section 7 discusses the key implications.

2. DATA

2.1. Sample Selection

To investigate whether variations in the plateau decay index reflect different GRB populations, we need a large, uniformly selected sample with well defined X-ray plateaus. The X-Ray Telescope (XRT) onboard *Neil Gehrels Swift Observatory* has detected over 1700 GRBs (Gehrels et al. 2004), and the corresponding X-ray light curves and spectra are publicly available through the *Swift*-XRT Repository¹ (Evans et al. 2007, 2009).

Tang et al. (2019) systematically analyzed all *Swift*/XRT GRBs observed between March 2005 and August 2018, aiming to study potential empirical relations involving plateau parameters. Their sample selection followed four criteria: (i) the temporal index of the plateau should be in the range -1.0 to $+1.0$; (ii) adequate data are available to define the plateau clearly; (iii) no flares were observed during the plateau phase; and (iv) the redshift should be available. A total of 174 GRBs (including 7 short bursts) satisfied these requirements. Each light curve was fitted with the smoothly broken power-law function (Liang et al. 2007; Li et al. 2012; Yi et al. 2016)

$$F_X(t) = F_{X,0} \left[\left(\frac{t}{T_{a,obs}} \right)^{\alpha_1 \omega} + \left(\frac{t}{T_{a,obs}} \right)^{\alpha_2 \omega} \right]^{-1/\omega}, \quad (1)$$

¹ https://www.swift.ac.uk/xrt_curves/

where α_1 and α_2 denote the temporal slopes before and after the break, $T_{\text{a,obs}}$ is the observed break time, ω sets the smoothness of the transition, and $F_{\text{X,0}} \cdot 2^{-1/\omega}$ corresponds to the flux at $T_{\text{a,obs}}$. The best-fit parameters were obtained via a Markov Chain Monte Carlo (MCMC) procedure.

Following a similar methodology, [Deng et al. \(2023\)](#) reanalyzed all *Swift*/XRT GRBs detected between March 2005 and May 2022, fixing the smoothness parameter to $\omega = 1$. To expand the sample size as far as possible, they included GRBs partially overlapped by X-ray flares. The flare intervals were excluded during the fitting procedure. This treatment is reasonable in light of more recent results (e.g., [Dereli-Bégué et al. 2025](#)), which indicate that X-ray flares originate from a process different from the plateau emission. As a result, they added 36 more GRBs with measured redshifts into the plateau sample, including 2 short bursts (GRB 090426 and GRB 100724A).

In this study, we further examined all *Swift*/XRT GRBs observed between June 2022 and August 2025 based on data from the *Swift*/XRT Repository, following the same selection criteria as [Deng et al. \(2023\)](#). This yielded 17 new GRBs with measured redshifts. Two short bursts (GRB 231117A and GRB 250221A) were excluded since we mainly concentrate on long events. The remaining 15 long GRBs were fitted with Eq. (1) using an MCMC method, and their best-fit parameters are listed in Table 1.

Given the systematic differences between long and short GRBs ([Margutti et al. 2013](#)) and the small number of short bursts, we restricted our study only to long GRBs. In total, we collected 216 long GRBs (167 from [Tang et al. \(2019\)](#), 34 from [Deng et al. \(2023\)](#), and 15 newly added here). To give a more strict definition for the plateau phase, here we require that the temporal index should be in the range of $-0.5 - +0.5$. This yields 185 GRBs, which constitute our final plateau sample.

Table 1. Key parameters of the 15 long *Swift* GRBs with an X-ray Plateau (after June 2022).

GRB name	z	T_{90}	$\log(F_{\text{X,0}}/10^{-12})$	$\log(T_{\text{a}}/10^3)$	α_1	α_2	Γ	$\log(L_{\text{X}}/10^{47})$	* Reference of z
(1)	(2)	(3)	(4)	(5)	(6)	(7)	(8)	(9)	(10)
220611A	2.36	57	$0.35^{+0.05}_{-0.03}$	$1.97^{+0.03}_{-0.06}$	$0.23^{+0.03}_{-0.03}$	$1.55^{+0.07}_{-0.08}$	1.9	$-0.35^{+0.05}_{-0.03}$	1
220813A	0.82	$\sim 30^b$	$1.13^{+0.25}_{-0.34}$	$0.53^{+0.42}_{-0.37}$	$0.26^{+0.18}_{-0.28}$	$1.16^{+0.12}_{-0.1}$	2	$-0.66^{+0.25}_{-0.34}$	2
230116D	3.81	41	$0.87^{+0.36}_{-0.33}$	$0.85^{+0.26}_{-0.34}$	$0.34^{+0.22}_{-0.4}$	$2.09^{+0.61}_{-0.36}$	1.76	$0.56^{+0.36}_{-0.33}$	3
230414B	3.57	25.98	$0.4^{+0.11}_{-0.09}$	$1.73^{+0.07}_{-0.08}$	$0.00^{+0.13}_{-0.16}$	$2.9^{+0.45}_{-0.37}$	2.02	$0.2^{+0.11}_{-0.11}$	4
230818A	2.42	9.82	$0.67^{+0.21}_{-0.14}$	$1.14^{+0.12}_{-0.2}$	$0.41^{+0.08}_{-0.13}$	$1.97^{+0.24}_{-0.22}$	2	$0.05^{+0.21}_{-0.14}$	5
240419A	5.18	3	$1.17^{+0.15}_{-0.25}$	$0.24^{+0.28}_{-0.23}$	$-0.07^{+0.3}_{-0.35}$	$1.4^{+0.2}_{-0.17}$	2.18	$1.48^{+0.15}_{-0.25}$	6
240529A	2.7	160.67	$1.91^{+0.03}_{-0.03}$	$1.27^{+0.02}_{-0.02}$	$0.11^{+0.04}_{-0.04}$	$2.29^{+0.06}_{-0.06}$	2.14	$1.48^{+0.03}_{-0.03}$	7
241010A	0.98	30.86	$1.56^{+0.08}_{-0.08}$	$1.06^{+0.09}_{-0.09}$	$0.18^{+0.04}_{-0.05}$	$1.53^{+0.06}_{-0.06}$	1.91	$-0.06^{+0.08}_{-0.08}$	8
241026A	2.79	25.2	$1.21^{+0.08}_{-0.08}$	$1.58^{+0.07}_{-0.07}$	$0.3^{+0.03}_{-0.04}$	$2.07^{+0.13}_{-0.12}$	1.86	$0.66^{+0.08}_{-0.08}$	9, 10
250101A	2.49	34.19	$1.07^{+0.25}_{-0.15}$	$0.79^{+0.16}_{-0.28}$	$0.34^{+0.07}_{-0.15}$	$1.48^{+0.12}_{-0.12}$	2.04	$0.5^{+0.25}_{-0.15}$	11, 12
250108B	2.2	229.66	$0.81^{+0.07}_{-0.27}$	$1.06^{+0.49}_{-0.19}$	$-0.22^{+0.43}_{-0.45}$	$0.95^{+0.12}_{-0.07}$	2.07	$0.12^{+0.07}_{-0.27}$	13
250114A	4.73	293.89	$0.27^{+0.13}_{-0.12}$	$1.5^{+0.08}_{-0.09}$	$0.5^{+0.1}_{-0.13}$	$3.58^{+0.51}_{-0.48}$	1.85	$0.23^{+0.13}_{-0.12}$	14
250129A	2.15	262.25	$1.16^{+0.08}_{-0.1}$	$0.97^{+0.13}_{-0.12}$	$-0.12^{+0.14}_{-0.15}$	$1.38^{+0.1}_{-0.08}$	1.94	$0.39^{+0.08}_{-0.1}$	15, 16
250424A	0.31	19.03	$2.14^{+0.06}_{-0.07}$	$0.78^{+0.1}_{-0.09}$	$0.05^{+0.06}_{-0.07}$	$1.16^{+0.03}_{-0.03}$	2.07	$-0.65^{+0.06}_{-0.07}$	17
250430A	0.77	9.17	$1.68^{+0.13}_{-0.29}$	$0.02^{+0.33}_{-0.22}$	$-0.27^{+0.47}_{-0.46}$	$1.73^{+0.93}_{-0.68}$	1.89	$-0.2^{+0.13}_{-0.29}$	18

Note. – Column (1): GRB name; (2): redshift; (3): duration from *Swift*/BAT in the 15 – 150 keV energy band; ^bGRB 220813A showed a single-peaked structure with a duration of about 30 s ([Bernardini et al. 2022](#)); (4): the flux at the end of the plateau is $F_{\text{X,0}}/2$; (5): the break time in the observer’s frame; (6): temporal power-law decay index of the plateau phase; (7): temporal power-law decay index of the post break segment; (8): photon index of the X-ray spectrum; (9): the isotropic X-ray luminosity at the break time after the K -correction; (10): references for the redshift measurement.

* 1.[Schneider et al. \(2022\)](#); 2.[Fausey et al. \(2022\)](#); 3.[Moskvitin et al. \(2023\)](#); 4.[Agui Fernandez et al. \(2023\)](#); 5.[Malesani et al. \(2023\)](#); 6.[Schneider et al. \(2024\)](#); 7.[de Ugarte Postigo et al. \(2024\)](#); 8.[Malesani et al. \(2024\)](#); 9.[Moskvitin et al. \(2024\)](#); 10.[Izzo et al. \(2024\)](#); 11.[Zhu et al. \(2025\)](#); 12.[Li et al. \(2025\)](#); 13.[Malesani et al. \(2025a\)](#); 14.[Malesani et al. \(2025b\)](#); 15.[Schneider et al. \(2025\)](#); 16.[Izzo et al. \(2025\)](#); 17.[Saccardi et al. \(2025\)](#); 18.[Garnichey et al. \(2025\)](#)

2.2. Sub-samples and Statistical Properties

We notice that the X-ray luminosity is not strictly constant during the plateau phase. It can either decrease or increase slightly, which is reflected in the variation of the plateau temporal index α_1 . To investigate whether such a behavior is due to different mechanisms, we divide the 185 long GRBs into three subsamples by considering the value of α_1 : bursts with $-0.5 < \alpha_1 \leq -0.1$ are called the *Rising* group, those with $-0.1 < \alpha_1 \leq 0.1$ are the *Flat* group, and those with $0.1 < \alpha_1 \leq 0.5$ are the *Decaying* group. The three subsamples have a rising, flat, or decaying plateau, respectively. Figure 1 shows a representative X-ray light curve of each group, together with the best-fit curve. In this way, the *Rising*, *Flat*, and *Decaying* subsamples contain 16, 75, and 94 GRBs, respectively.

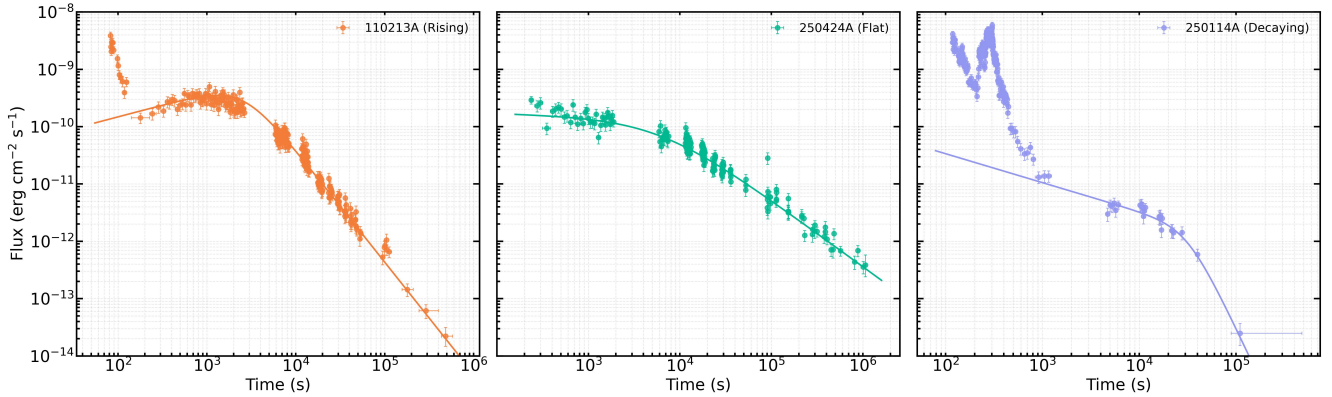


Figure 1. Exemplar X-ray afterglow light curves of GRBs 110213A, 250424A, and 250114A, which has a rising, flat, and decaying plateau, respectively. The solid curves show the best-fit results by using Equation (1) with the MCMC method.

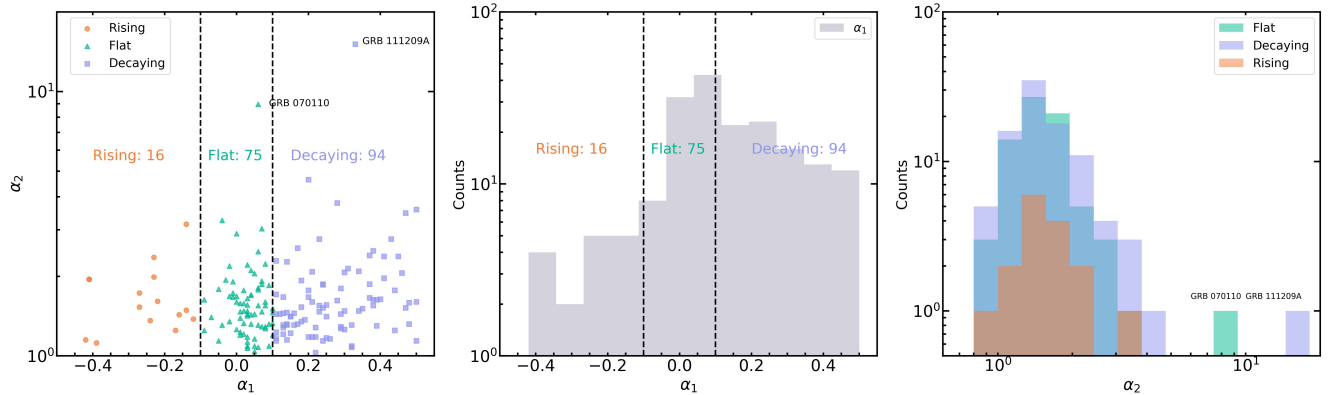


Figure 2. Distributions of the temporal indices during (α_1) and after (α_2) the plateau phase for the three groups. **Left:** α_2 plotted versus α_1 , where the filled circles, triangles and squares represent the *Rising*, *Flat* and *Decaying* subsamples, respectively. **Middle:** histogram of α_1 for all the plateau GRBs. **Right:** histograms of α_2 for the three groups.

The overall distribution of α_1 and α_2 is shown in Figure 2. The left panel plots α_1 versus α_2 . We see that these two indices are generally independent of each other. In fact, we have explored any potential correlation between α_1 and α_2 and obtained a Pearson coefficient of $r = 0.11$, with a significance of $p \simeq 0.13$, indicating a very weak and statistically insignificant correlation. In the middle panel, the distribution of α_1 is not symmetrical, but slightly skewed toward positive values, peaking at $\alpha_1 \simeq 0.1$, consistent with the results of Tang et al. (2019). In the right panel, we see that α_2 lies mainly in $0.8 \lesssim \alpha_2 \lesssim 4.0$. There are no clear difference in the distribution of α_2 for the three subsamples.

A small number of GRBs display an exceptionally steep decay rate after the plateau, including GRB 070110 ($\alpha_2 \approx 8.95$), GRB 100219A ($\alpha_2 \approx 4.64$), GRB 100902A ($\alpha_2 \approx 4.69$), GRB 111209A ($\alpha_2 \approx 15.11$) and GRB 170714A ($\alpha_2 \approx 4.97$). These rapid declines are typical of internal plateau bursts, potentially due to the sudden termination of the central-engine activity (Troja et al. 2007; Lyons et al. 2010; Chen et al. 2017; Beniamini & Mochkovitch 2017).

Figure 2 also highlights two representative examples – GRB 070110 and GRB 111209A – to illustrate their extreme α_2 values.

We have calculated the difference between α_1 and α_2 , i.e. $\Delta\alpha = \alpha_2 - \alpha_1$. It is found that the average difference is $\langle \Delta\alpha \rangle = 1.598$, which is consistent with earlier results of Liang et al. (2007) (1.11 ± 0.39) and Tang et al. (2019) (1.4 ± 0.3). Given the relatively narrow distribution of α_2 and its weak correlation with α_1 , classifying GRBs into *Rising*, *Flat*, and *Decaying* subsamples based on α_1 alone is reasonable.

2.3. Plateau Luminosity

Based on the fitted $F_{X,0}$ parameter, the isotropic X-ray luminosity at the end of the plateau can be calculated as

$$L_X = 4\pi D_L^2(z) \frac{F_{X,0}}{2} K, \quad (2)$$

where K is the K -correction factor, and $D_L(z)$ is the luminosity distance,

$$D_L(z) = (1+z) \frac{c}{H_0} \int_0^z \frac{dz'}{\sqrt{\Omega_M(1+z')^3 + \Omega_\Lambda}}, \quad (3)$$

with c being the speed of light. Here, we adopt a flat Lambda Cold Dark Matter (Λ CDM) cosmology with $H_0 = 67.3 \text{ km s}^{-1} \text{ Mpc}^{-1}$, $\Omega_M = 0.315$, and $\Omega_\Lambda = 1 - \Omega_M$ (Planck Collaboration et al. 2014, 2020).

The K -correction (Bloom et al. 2001) is calculated as

$$K = \frac{\int_{E_1/(1+z)}^{E_2/(1+z)} E N(E) dE}{\int_{E_1}^{E_2} E N(E) dE}, \quad (4)$$

where (E_1, E_2) denotes the energy band of the detector. Considering the relatively narrow energy coverage of *Swift*/XRT, we approximate the photon spectrum by a simple power law, $N(E) = N_0 E^{-\Gamma}$, where Γ is the photon index measured by *Swift*/XRT. The values of Γ are taken from the *Swift* GRB online catalogue². With this power-law spectrum, the isotropic X-ray luminosity simplifies to

$$L_X = \frac{4\pi D_L^2(z)}{(1+z)^{2-\Gamma}} \frac{F_{X,0}}{2}, \quad (5)$$

after considering the K -correction.

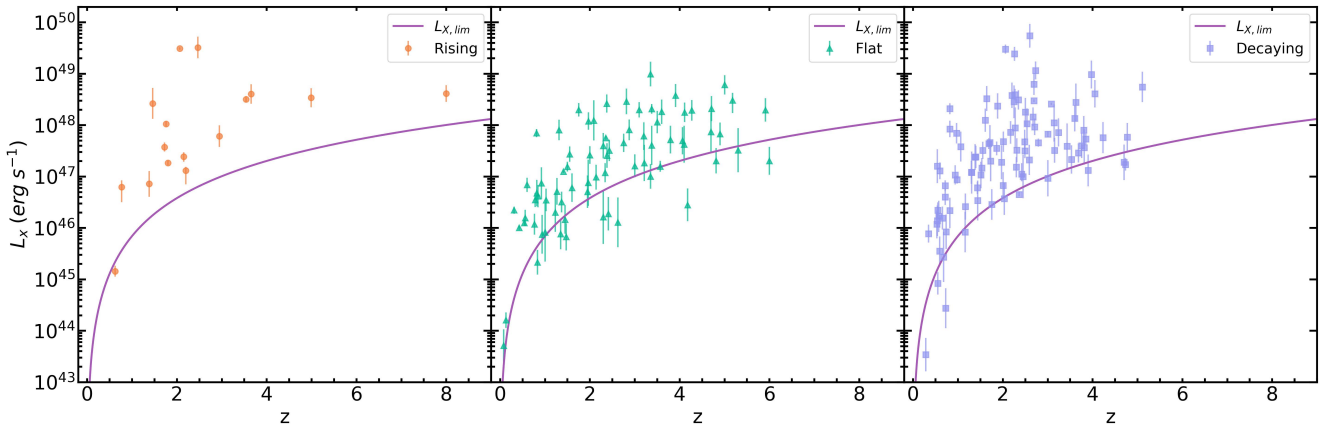


Figure 3. X-ray plateau luminosity plotted versus redshift for the three subsamples. The solid curves are plotted by assuming a flux limit of $\log(F_{\text{lim}}/1 \text{ erg cm}^{-2} \text{ s}^{-1}) = -11.9$ (Khatiya et al. 2025), which will be taken as the detection threshold to ensure sample completeness in our subsequent calculations.

² https://swift.gsfc.nasa.gov/archive/grb_table/

In Table 1, we have also listed the derived plateau luminosity for the 15 new long GRBs observed by *Swift*/BAT between June 2022 and August 2025. For the other earlier long GRBs with X-ray plateaus, the isotropic luminosity data are directly taken from Tang et al. (2019) and Deng et al. (2023). The distribution of L_X is shown in Figure 3 for the three subsamples. Following Khatiya et al. (2025), we have assumed a flux threshold of $\log(F_{\text{lim}}/1 \text{ erg cm}^{-2} \text{ s}^{-1}) = -11.9$ to ensure sample completeness in our subsequent analysis. The derived limiting curve is also shown in Figure 3. We see that nearly all rising-plateau GRBs are located above the detection threshold, while a small number of events in the flat and decaying subsamples are below the threshold. Such a distribution hints that the rising plateaus preferentially occur in systems with a stronger engine power.

3. MODELING THE EVENT RATE

We have grouped the 185 long GRBs with well-defined X-ray plateaus into three subsamples according to their temporal index α_1 . In this section, we compare these subsamples in terms of their luminosity function, redshift distribution, and event rate to examine whether the various plateau behaviors are due to different intrinsic physical processes.

To derive the intrinsic luminosity function and event rate, corrections for redshift evolution and observational biases are required. Malmquist bias and instrumental flux truncation can induce artificial luminosity evolution and selection effects. To mitigate these, we employ the non-parametric Lynden-Bell C^- method (Lynden-Bell 1971), which provides an unbiased estimate of the intrinsic event rate distribution in flux-limited samples.

The C^- estimator is a non-parametric maximum-likelihood approach developed for randomly truncated data and has been widely adopted for GRB event rate estimation (Yu et al. 2015a; Pescalli et al. 2016; Zhang & Wang 2018; Liu et al. 2021; Dong et al. 2022, 2023, 2025; Champati et al. 2025). It is also effective in correcting for selection biases and parameter evolution (Efron & Petrosian 1992; Dainotti et al. 2013, 2017; Xu et al. 2021) and underpinning more advanced statistical inferences such as two-sample test, correlation, linear regression, and Bayesian analysis (Efron & Petrosian 1992; Feigelson & Babu 2012; Dörre & Emura 2019).

Before applying the C^- method, the truncation boundary defined by the detector sensitivity must be specified. Khatiya et al. (2025) followed the procedure outlined in Dainotti et al. (2021), which examine the completeness of their plateau GRB dataset to select the optimal flux threshold value. They found that different flux thresholds yield broadly similar GRB event rates, a result that was also confirmed by Dong et al. (2022) and Liu et al. (2025). In this study, we adopt a flux limit of $\log(F_{\text{lim}}/1 \text{ erg cm}^{-2} \text{ s}^{-1}) = -11.9$, following their choice. The sensitivity curve is then calculated as $L_{X,\text{lim}} = 4\pi D_L^2(z)F_{\text{lim}}/(1+z)^{2-\Gamma_{\text{avg}}}$, as shown by the solid line in Figure 3, where $\Gamma_{\text{avg}} \simeq 1.99$ is the average photon index.

An additional requirement of the C^- method is that the luminosity (L_X) and redshift (z) should be statistically independent, implying no intrinsic luminosity evolution. We test and remove such evolution using the non-parametric Efron-Petrosian (EP) method (Efron & Petrosian 1992). After the de-evolved data set is ready, the C^- method can be applied to reconstruct the intrinsic luminosity and redshift distributions with various biases being removed as far as possible (Dainotti et al. 2013).

3.1. EP Method

The EP method (also known as the τ -statistic test; Efron & Petrosian 1992) is employed to remove the redshift evolution of luminosity, i.e., the intrinsic correlation between L_X and z . Following Khatiya et al. (2025), we assume that the observed luminosity evolves with redshift as $L_X \propto (1+z)^k$, where k is a constant quantifying the degree of evolution. Once k is determined, the evolution-corrected luminosity can be expressed as $L'_X = L_X/(1+z)^k$. This correction yields an independent parameter pair (z, L'_X) , such that the GRB distribution function can be factorized as $\Psi(L'_X, z) = \psi(L'_X) \phi(z)$, where $\psi(L'_X)$ and $\phi(z)$ represent the luminosity function and redshift distribution, respectively.

To estimate k , each GRB data point $(z_i, L_{X,i})$ is transformed into $(z_i, L'_{X,i})$ for a given trial k . For the i th GRB, we define a comparable data set

$$J_i = \{ j \mid L'_{X,j} \geq L'_{X,i}, z_j \leq z_i^{\text{max}} \}, \quad (6)$$

where z_i^{max} is the maximum redshift at which a burst with luminosity $L'_{X,i}$ can be detected by *Swift*/XRT. The number of GRBs in this region is denoted by n_i , and the number of sources with $z \leq z_i$ is R_i . The τ statistic is defined as

$$\tau = \frac{\sum_i (R_i - T_i)}{\sqrt{\sum_i V_i}}, \quad (7)$$

where $T_i = (1 + n_i)/2$ and $V_i = (n_i^2 - 1)/12$ are the expected mean and variance of R_i , respectively.

If luminosity and redshift are independent, R_i should be uniformly distributed between 1 and n_i , giving $\tau \approx 0$. Otherwise, the trial value of k is adjusted and the process repeated until $\tau = 0$ is achieved, yielding the best-fit evolution index. Using this procedure, we find $k \simeq 5.53$ for the rising sample, $k \simeq 4.17$ for the flat sample, and $k \simeq 4.32$ for the decaying sample. The X-ray plateau luminosities are then corrected by dividing them by $(1 + z)^k$.

3.2. Lynden–Bell’s C^- Method

The Lynden–Bell’s C^- method offers an effective approach for recovering the intrinsic bivariate distributions of astronomical sources from truncated data sets. For each GRB, we define a comparable data set

$$J'_i = \{j \mid L'_{X,j} \geq L'_{X,i}^{\min}, z_j < z_i\}, \quad (8)$$

where $L'_{X,i}^{\min}$ is the minimum detectable luminosity at z_i , and M_i denotes the number of GRBs contained in J'_i .

According to the C^- formalism, the cumulative luminosity function of GRB plateaus can be estimated as

$$\psi(L'_{X,i}) = \prod_{j > i} \left(1 + \frac{1}{N_j}\right), \quad (9)$$

where the product runs over all GRBs with de-evolved luminosities $L'_{X,j} > L'_{X,i}$. Similarly, the cumulative redshift distribution is given by

$$\phi(z_i) = \prod_{j < i} \left(1 + \frac{1}{M_j}\right), \quad (10)$$

where the product runs over all GRBs with $z_j < z_i$. The comoving event rate of GRBs is then obtained as

$$\rho(z) = (1 + z) \frac{d\phi(z)}{dz} \left[\frac{dV(z)}{dz} \right]^{-1}, \quad (11)$$

where the factor $(1 + z)$ accounts for cosmological time dilation, and $dV(z)/dz$ is the differential comoving volume element (Khokhriakova & Popov 2019):

$$\frac{dV(z)}{dz} = \frac{c}{H_0} \frac{4\pi D_L^2(z)}{(1 + z)^2} \frac{1}{\sqrt{(1 - \Omega_M) + \Omega_M(1 + z)^3}}. \quad (12)$$

4. RESULTS

In this section, we present our main results obtained for the rising, flat, and decaying subsamples. First, we compare the luminosity functions of the three groups. We then derive their redshift-dependent event rates and compare them with the cosmic star-formation rate (SFR) to explore potential links between the plateau GRBs and star-forming environments.

4.1. Luminosity Functions

Figure 4 presents the luminosity functions of the three subsamples, computed using Equation (9). Generally, all the three curves exhibit similar shapes, declining as the luminosity increases, with a shallow slope at low luminosity segment and a steeper drop at the high luminosity regime, with only minor fluctuations. The rising and flat subsamples extend to slightly lower luminosity segment than the decaying one, but the reasons are different. In the flat subsample, two nearby low-luminosity bursts pass the flux threshold (GRB 051109B at $z \approx 0.08$ and GRB 060614 at $z \approx 0.13$; Perley et al. 2006; Gehrels et al. 2006; Mangano et al. 2007), whereas the rising sample reaches a lower luminosity mainly because a stronger redshift-luminosity evolution correction (i.e., a larger k) is applied.

To better understand the luminosity function of each subsample, we have tried to fit it with both a Schechter model,

$$\psi(L) = \psi_* \left(\frac{L}{L_*} \right)^\gamma \exp \left(-\frac{L}{L_*} \right), \quad (13)$$

and a smoothly broken power-law (SBPL) model,

$$\psi(L) = \psi_0 \left[\left(\frac{L}{L_{\text{break}}} \right)^{A_1 w} + \left(\frac{L}{L_{\text{break}}} \right)^{A_2 w} \right]^{-1/w}, \quad (14)$$

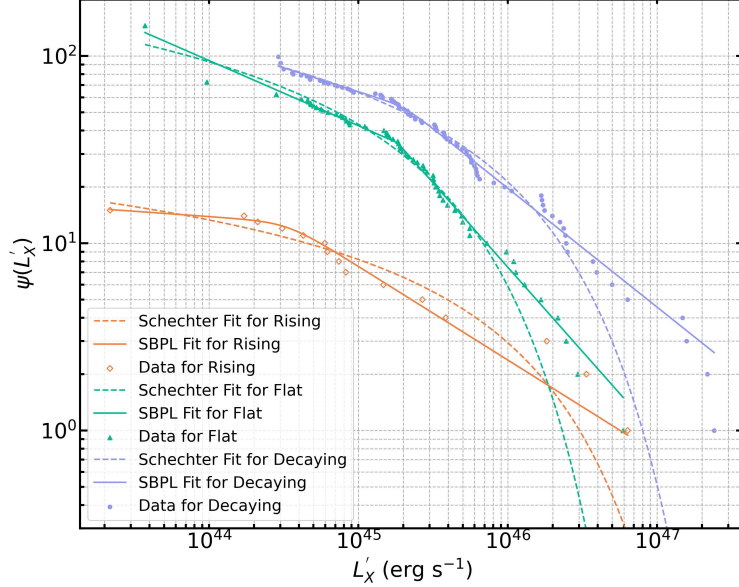


Figure 4. Luminosity functions of the three subsamples. The data points have been calculated by using Equation (9), where the diamonds, triangles and filled circles represent the rising, flat and decaying subsamples, respectively. The dashed line denote the best-fit Schechter function for each subsample, while the solid curve shows the best-fit SBPL model. The corresponding best-fit parameters are listed in Table 2.

Table 2. Best-fit parameters of the Schechter function and the smoothly broken power-law function.

Schechter Function				
Sample	ψ_*	L_* (10^{46} erg s $^{-1}$)	γ	R^2
(1)	(2)	(3)	(4)	(5)
Rising	2.82 ± 1.20	4.12 ± 3.42	-1.95 ± 0.10	0.9284
Flat	22.4 ± 4.25	1.15 ± 0.27	-2.00 ± 0.06	0.9467
Decaying	20.3 ± 2.47	4.01 ± 0.65	-2.00 ± 0.03	0.9859
Smoothly Broken Power-law Function				
Sample	L_{break} (10^{45} erg s $^{-1}$)	A_1	A_2	R^2
(1)	(2)	(3)	(4)	(5)
Rising	0.34 ± 1.19	0.06 ± 0.12	0.5 ± 0.03	0.9810
Flat	1.83 ± 0.17	0.35 ± 0.01	0.90 ± 0.09	0.9769
Decaying	2.06 ± 0.15	0.25 ± 0.01	0.64 ± 0.02	0.9930

where L_* and L_{break} are the characteristic luminosity and γ , A_1 and A_2 denote the slopes. We then compare the goodness of fit of these two models.

The best-fit curves of the two kinds of models are shown in Figure 4, with the corresponding parameters listed in Table 2. The SBPL model is generally better than the Schechter function, with a correlation coefficient in the range of $R^2 \approx 0.98 - 0.993$, compared to $R^2 \approx 0.93 - 0.986$ for the Schechter model. Note that the sample size of the rising group is relatively small, so the corresponding fits are less reliable and the model parameters are not well constrained. Despite minor fluctuations in the original data points, the smooth best-fit functions adequately capture the overall trends relevant for comparison. In short, we see that the luminosity functions are largely similar for the three subsamples, supporting a common origin for plateau GRBs that is basically independent of the observed plateau slope.

4.2. Event Rate

Figure 5 shows the normalized cumulative redshift distributions of the three subsamples, calculated using Equation (10). Nearly all GRBs are in the range of $0 < z \lesssim 6$. The only outlier is GRB 090423 ($z \approx 8$; Tanvir et al.

2009; Salvaterra et al. 2009), which belongs to the rising-plateau subsample. Although its rest-frame duration is short ($T_{90,\text{rest}} \sim 1.1\text{s}$), it is widely believed to be a collapsar-type long GRB when its observational features are synthesized.

Figure 6 illustrates the event rate of the three subsamples, computed by using Equation (11). The event rate is scaled by an arbitrary factor for direct comparison with the SFR. The three groups exhibit similar redshift evolution: the event rate is weakly dependent on the redshift, and is largely consistent with the observed SFR data in the redshift range of 1–5. Such a close similarity among the rising, flat, and decaying groups suggests that the X-ray plateau emission is most likely governed by a common mechanism. Otherwise, even if multiple physical channels contribute to the plateau formation, their relative contributions should not vary significantly across the three categories. Additionally, the agreement with the cosmic SFR further suggests that GRBs exhibiting a plateau phase are predominantly residing in active star-forming environments, supporting their connection with the death of massive stars.

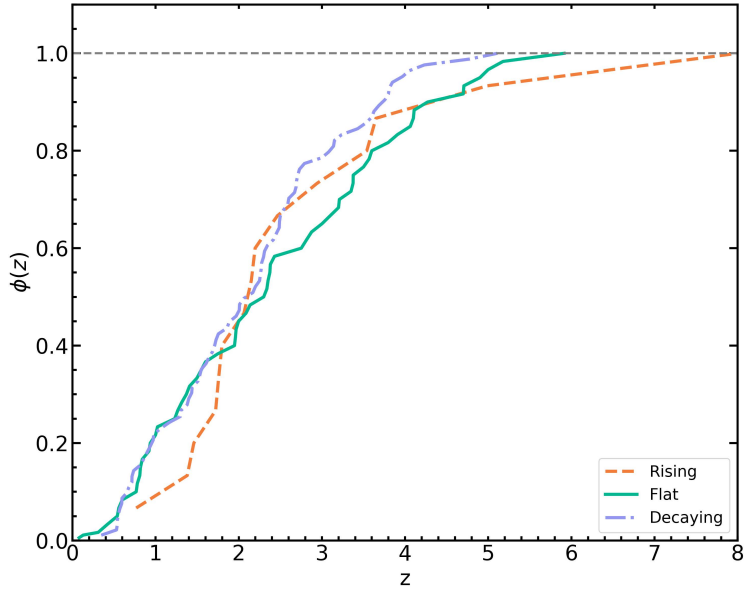


Figure 5. Normalized cumulative redshift distributions of the three subclasses. The dashed, solid, and dash-dotted lines represent the rising, flat, and decaying plateau groups, respectively.

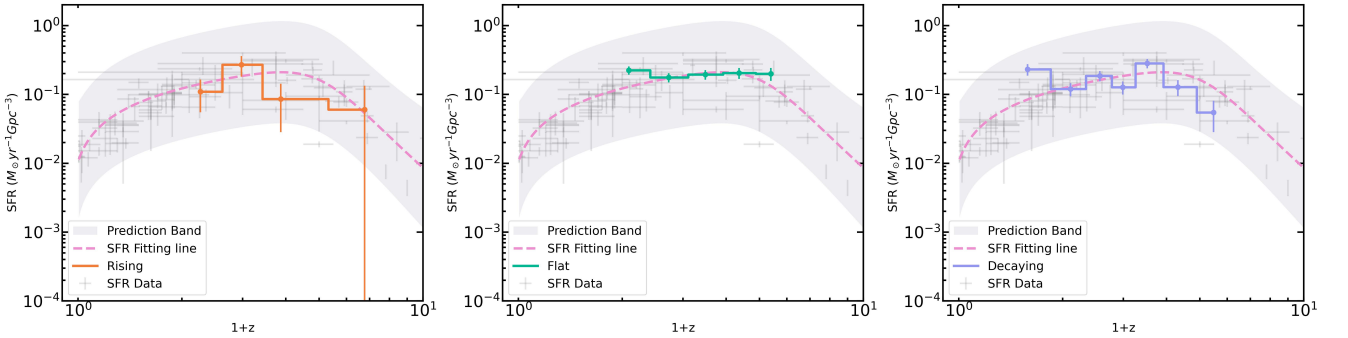


Figure 6. Event rates of the rising, flat, and decaying plateau subsamples. Step lines show the inferred event rates; scatter data points show observed SFR. The dashed lines show the best-fit SFR curve and the gray shaded region marks its 99% confidence level, adopted from Dong et al. (2022).

5. SLOPE CRITERIA AND DEFINITION OF THE SUBSAMPLES

In our study, we have divided GRBs with X-ray plateaus into *Rising* ($-0.5 < \alpha_1 \leq -0.1$), *Flat* ($-0.1 < \alpha_1 \leq 0.1$), and *Decaying* ($0.1 < \alpha_1 \leq 0.5$) groups. Across these groups, it is found that the luminosity functions, cumulative

redshift distributions, and event rates exhibit similar shapes. The similarity suggests that the plateau GRBs with different plateau slopes may have a common origin.

In the previous analysis, the intermediate group (i.e. the *Flat* plateau subsample) is defined by a slope criteria of 0.1. That is, the flat group meet the requirement of $-0.1 < \alpha_1 \leq 0.1$. One concern is whether the result is dependent on the choice of the criteria. To test this, we performed a Monte Carlo analysis in which the threshold of $|\alpha_1|$ (originally 0.1) varies uniformly between 0.05 and 0.15. The range of 0.05 – 0.15 was chosen to ensure that each group contains enough GRBs for meaningful statistics, particularly for the rising group. For each of the randomly evaluated threshold, the sample was reclassified and the luminosity functions, redshift distributions, and event rates of the subsamples were recomputed. We repeated the process 10,000 times, which yielded 10,000 realizations of the key features for the three groups, allowing for a thorough assessment of the robustness of our results.

Figure 7 shows all Monte Carlo realizations, normalized for comparison. We see that for each subsample, the realizations cluster tightly, indicating that the luminosity function, redshift distribution, and event rate are insensitive to the precise choice of the slope criteria. The three subsamples also remain highly similar across all realizations. In particular, their normalized event rates are highly clustered and overlapped, which are quite flat for $z \lesssim 5$, consistent with the cosmic SFR. Our simulations demonstrate that the similarity among the three subsamples groups is robust and is not an artifact of the adopted boundaries of α_1 . Thus, GRBs with X-ray plateaus are governed by a common underlying mechanism although the plateau slope varies markedly.

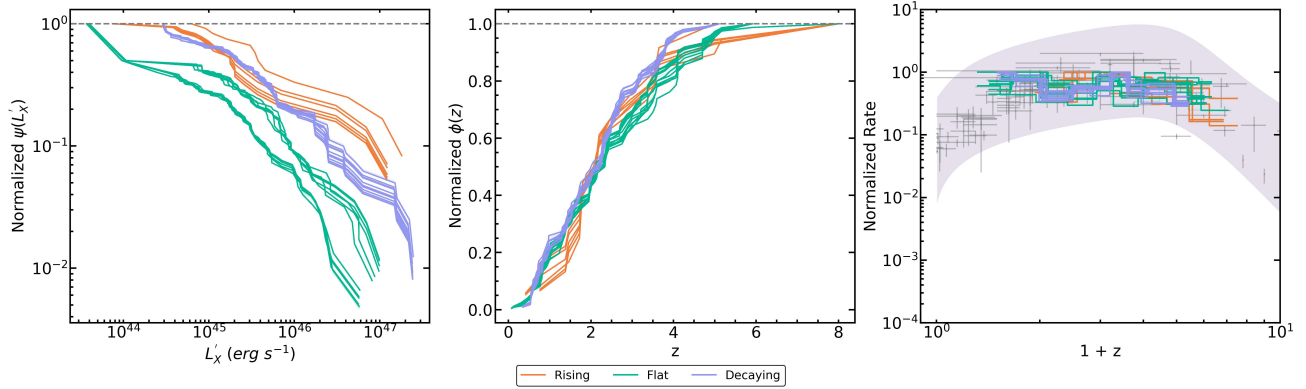


Figure 7. Results of 10,000 Monte Carlo simulations for the slope criteria. The left, middle, and right panels show the normalized luminosity functions, cumulative redshift distributions and event rates, respectively. The orange, green, and purple lines correspond to the rising-, flat-, and decaying-plateau subsamples.

6. CONCLUSION

The origin of the X-ray plateau in GRB afterglows remains uncertain, with numerous models proposed and no consensus yet established. Motivated by the possibility that the timing index α_1 of the plateau may encode information about the underlying mechanism, we examined whether different values of α_1 correspond to different plateau populations.

A large sample of 185 *Swift*/XRT GRBs with a well-defined plateau is compiled in this study. They are further divided into rising, flat, and decaying subsamples using a threshold of ± 0.1 . The luminosity function, cumulative redshift distribution and event rate are derived for each group. It is found that these three functions exhibit similar behavior across the subsamples, with no statistically significant differences. A Monte Carlo test in which the slope criteria varies over a broad range further confirms that the similarity is robust and is not an artifact of the particular choice of the slope criteria.

Our results indicate that the plateau decay index alone does not delineate distinct physical subclasses. Instead, GRBs with a rising, flat, or decaying X-ray plateau exhibit statistically indistinguishable properties, strongly pointing to a unified mechanism for the plateau rather than drawing from different progenitors or environments.

7. DISCUSSION

Our population-level analysis shows no distinct separation among rising, flat, and decaying subsamples. The shallow-decay index exhibits a continuous and uni-modal distribution, consistent with previous studies involving plateau

luminosity, isotropic energy, break time, and Dainotti-relation residuals (Dainotti et al. 2010; Tang et al. 2019; Yi et al. 2022). These results suggest that X-ray plateaus form a single, continuous population rather than discrete subtypes.

We have also taken all the 185 X-ray plateau GRBs as a single sample and recomputed the event rate. The result is plotted in Figure 8. We see that the event rate is again independent on the redshift as long as $z < 4$, which is consistent with that of the rising, flat, and decaying subsamples. It generally follows the SFR, with only a mild low-redshift deviation, similar to the feature reported by Khatiya et al. (2025), who interpreted the deviation as a consequence of GRBs being biased tracers of star formation. Note that comparing with the study of Khatiya et al. (2025), a more stringent plateau-slope criterion of $|\alpha_1| \leq 0.5$ was applied in our sample.

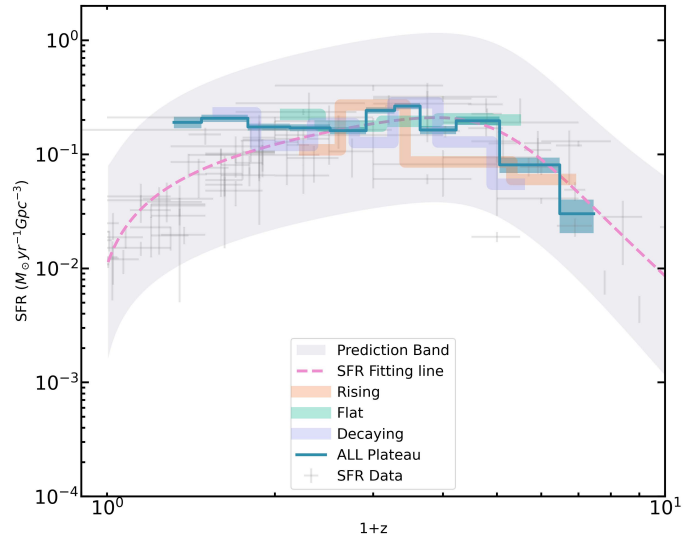


Figure 8. Event rates derived from the full sample of 185 X-ray plateau GRBs. The solid step line shows the event rate of the full plateau sample, while the shaded step lines represent the event rates of the rising, flat, and decaying groups, respectively.

Du et al. (2024) recently analyzed 310 *Swift* GRB X-ray afterglows and divided them into four temporal categories based on the presence of flares, plateaus, and breaks. According to their classification, the Category I GRBs are featured by an X-ray flare along with two breaks; Category II GRBs have two breaks and a plateau; Category III GRBs have two breaks but without a plateau; Category IV GRBs have no breaks and no plateaus. They found that both the γ -ray hardness ratio and the peak energy of bursts of types I, II, and III are identically distributed and are significantly lower than the corresponding parameters of type IV bursts in statistics. Our sample is somewhat similar to their Category II. The difference is that we further divide this sample into three subsamples by considering the plateau slope.

Our population-level analysis indicates that the plateau slope α_1 does not delineate separate GRB populations at the macro level. Instead, the difference in α_1 likely reflects micro-physical variations within a unified central-engine framework. For instance, a continuous variation in the magnetar spin period, surface magnetic field, or ellipticity naturally produces a broad spectrum of plateau slopes (Lyons et al. 2010). Event-level analyses also reveals smooth, correlated variations among these parameters (Lan et al. 2025), providing a physical basis for the observed α_1 continuity. In the future, a larger, well-sampled plateau dataset could enable more in-depth population-level constraints on the central-engine and energy-injection efficiency.

Recently, several groups applied the Lynden–Bell’s C^- method to fast X-ray transients (FXTs) detected by the Einstein Probe to estimate their event rates, although the current samples are still limited (Guo et al. 2025; Li et al. 2026). It was found that the FXT event rate is comparable to that of typical long GRBs, suggesting a possible connection between the two populations. With the recent release of an expanded Einstein Probe FXT catalog (Wu & EP Collaboration et al. 2025), including sources exhibiting extended plateau-like evolution in their soft X-ray light curves, the growing uniform sample may enable population-level analysis to constrain the origin of plateau-containing FXTs.

8. ACKNOWLEDGEMENTS

This study was supported by the National Natural Science Foundation of China (Grant No. 12233002, 12273113), by the National Key R&D Program of China (2021YFA0718500), by the China Postdoctoral Science Foundation (No. 2025M783225), by the Shandong Provincial Natural Science Foundation (No. ZR2023MA049), and by the Postgraduate Research & Practice Innovation Program of Jiangsu Province (No. KYCX25_0197). Y.F.H. acknowledges the support from the Xinjiang Tianchi Program. J.J.G. acknowledges support from the Youth Innovation Promotion Association (2023331).

REFERENCES

Agui Fernandez, J. F., Thoene, C. C., de Ugarte Postigo, A., et al. 2023, GRB Coordinates Network, 33629, 1

Ascenzi, S., Oganesyan, G., Salafia, O. S., et al. 2020, *A&A*, 641, A61, doi: [10.1051/0004-6361/202038265](https://doi.org/10.1051/0004-6361/202038265)

Beniamini, P., Duque, R., Daigne, F., & Mochkovitch, R. 2020, *MNRAS*, 492, 2847, doi: [10.1093/mnras/staa070](https://doi.org/10.1093/mnras/staa070)

Beniamini, P., & Mochkovitch, R. 2017, *A&A*, 605, A60, doi: [10.1051/0004-6361/201730523](https://doi.org/10.1051/0004-6361/201730523)

Bernardini, M. G., Brivio, R., Ferro, M., et al. 2022, GRB Coordinates Network, 32465, 1

Bloom, J. S., Frail, D. A., & Sari, R. 2001, *AJ*, 121, 2879, doi: [10.1086/321093](https://doi.org/10.1086/321093)

Champati, S., Petrosian, V., & Dainotti, M. G. 2025, arXiv e-prints, arXiv:2510.23945, doi: [10.48550/arXiv.2510.23945](https://doi.org/10.48550/arXiv.2510.23945)

Chen, W., Xie, W., Lei, W.-H., et al. 2017, *ApJ*, 849, 119, doi: [10.3847/1538-4357/aa8f4a](https://doi.org/10.3847/1538-4357/aa8f4a)

Dai, Z. G., & Lu, T. 1998, *PhRvL*, 81, 4301, doi: [10.1103/PhysRevLett.81.4301](https://doi.org/10.1103/PhysRevLett.81.4301)

Dainotti, M. G., Cardone, V. F., & Capozziello, S. 2008, *MNRAS*, 391, L79, doi: [10.1111/j.1745-3933.2008.00560.x](https://doi.org/10.1111/j.1745-3933.2008.00560.x)

Dainotti, M. G., Nagataki, S., Maeda, K., Postnikov, S., & Pian, E. 2017, *A&A*, 600, A98, doi: [10.1051/0004-6361/201628384](https://doi.org/10.1051/0004-6361/201628384)

Dainotti, M. G., Petrosian, V., & Bowden, L. 2021, *ApJL*, 914, L40, doi: [10.3847/2041-8213/abf5e4](https://doi.org/10.3847/2041-8213/abf5e4)

Dainotti, M. G., Petrosian, V., Singal, J., & Ostrowski, M. 2013, *ApJ*, 774, 157, doi: [10.1088/0004-637X/774/2/157](https://doi.org/10.1088/0004-637X/774/2/157)

Dainotti, M. G., Willingale, R., Capozziello, S., Fabrizio Cardone, V., & Ostrowski, M. 2010, *ApJL*, 722, L215, doi: [10.1088/2041-8205/722/2/L215](https://doi.org/10.1088/2041-8205/722/2/L215)

de Ugarte Postigo, A., Thoene, C. C., Agui Fernandez, J. F., et al. 2024, GRB Coordinates Network, 36574, 1

Deng, C., Huang, Y.-F., & Xu, F. 2023, *ApJ*, 943, 126, doi: [10.3847/1538-4357/acaefd](https://doi.org/10.3847/1538-4357/acaefd)

Deng, C., Huang, Y.-F., Kurban, A., et al. 2025, arXiv e-prints, arXiv:2511.11396, doi: [10.48550/arXiv.2511.11396](https://doi.org/10.48550/arXiv.2511.11396)

Dereli-Bégué, H., Pe'er, A., Bégué, D., Ryde, F., & Gowri, A. 2025, arXiv e-prints, arXiv:2512.07731, <https://arxiv.org/abs/2512.07731>

Dereli-Bégué, H., Pe'er, A., Ryde, F., et al. 2022, *Nature Communications*, 13, 5611, doi: [10.1038/s41467-022-32881-1](https://doi.org/10.1038/s41467-022-32881-1)

Dong, X.-F., Huang, Y.-F., Zhang, Z.-B., et al. 2025, *ApJ*, 993, 20, doi: [10.3847/1538-4357/ae04e7](https://doi.org/10.3847/1538-4357/ae04e7)

Dong, X. F., Li, X. J., Zhang, Z. B., & Zhang, X. L. 2022, *MNRAS*, 513, 1078, doi: [10.1093/mnras/stac949](https://doi.org/10.1093/mnras/stac949)

Dong, X. F., Zhang, Z. B., Li, Q. M., Huang, Y. F., & Bian, K. 2023, *ApJ*, 958, 37, doi: [10.3847/1538-4357/acf852](https://doi.org/10.3847/1538-4357/acf852)

Du, X. Y., Zhen, H. Y., Liu, J. X., et al. 2024, *ApJ*, 960, 77, doi: [10.3847/1538-4357/ad0f24](https://doi.org/10.3847/1538-4357/ad0f24)

Dörre, A., & Emura, T. 2019, Analysis of Doubly Truncated Data, An Introduction (Springer Singapore), doi: <https://doi.org/10.1007/978-981-13-6241-5>

Efron, B., & Petrosian, V. 1992, *ApJ*, 399, 345, doi: [10.1086/171931](https://doi.org/10.1086/171931)

Evans, P. A., Beardmore, A. P., Page, K. L., et al. 2007, *A&A*, 469, 379, doi: [10.1051/0004-6361:20077530](https://doi.org/10.1051/0004-6361:20077530)

—. 2009, *MNRAS*, 397, 1177, doi: [10.1111/j.1365-2966.2009.14913.x](https://doi.org/10.1111/j.1365-2966.2009.14913.x)

Fan, Y., & Piran, T. 2006, *MNRAS*, 369, 197, doi: [10.1111/j.1365-2966.2006.10280.x](https://doi.org/10.1111/j.1365-2966.2006.10280.x)

Fausey, H., Zhu, Z. P., D'Avanzo, P., et al. 2022, GRB Coordinates Network, 32471, 1

Feigelson, E. D., & Babu, G. J. 2012, Modern Statistical Methods for Astronomy (Cambridge University Press), doi: <https://doi.org/10.1017/CBO9781139015653>

Fraija, N., Kamenetskaia, B. B., Galván, A., & Dainotti, M. G. 2025, *MNRAS*, doi: [10.1093/mnras/staf1970](https://doi.org/10.1093/mnras/staf1970)

Fraija, N., Kamenetskaia, B. B., Galvan-Gomez, A., et al. 2022, *ApJ*, 933, 243, doi: [10.3847/1538-4357/ac714d](https://doi.org/10.3847/1538-4357/ac714d)

Garnichey, M., Saccardi, A., Schneider, B., et al. 2025, GRB Coordinates Network, 40301, 1

Gehrels, N., Chincarini, G., Giommi, P., et al. 2004, *ApJ*, 611, 1005, doi: [10.1086/422091](https://doi.org/10.1086/422091)

Gehrels, N., Norris, J. P., Barthelmy, S. D., et al. 2006, *Nature*, 444, 1044, doi: [10.1038/nature05376](https://doi.org/10.1038/nature05376)

Genet, F., Daigne, F., & Mochkovitch, R. 2007, *MNRAS*, 381, 732, doi: [10.1111/j.1365-2966.2007.12243.x](https://doi.org/10.1111/j.1365-2966.2007.12243.x)

Ghisellini, G., Ghirlanda, G., Nava, L., & Firmani, C. 2007, *ApJL*, 658, L75, doi: [10.1086/515570](https://doi.org/10.1086/515570)

Granot, J., & Kumar, P. 2003, *ApJ*, 591, 1086, doi: [10.1086/375489](https://doi.org/10.1086/375489)

—. 2006, *MNRAS*, 366, L13, doi: [10.1111/j.1745-3933.2005.00121.x](https://doi.org/10.1111/j.1745-3933.2005.00121.x)

Guglielmi, L., Stratta, G., Dall’Osso, S., et al. 2024, *A&A*, 692, A73, doi: [10.1051/0004-6361/202451877](https://doi.org/10.1051/0004-6361/202451877)

Guidorzi, C., Maccary, R., Maistrello, M., et al. 2025, *A&A*, 703, A101, doi: [10.1051/0004-6361/202556663](https://doi.org/10.1051/0004-6361/202556663)

Guo, Y., Zeng, H., Wei, J., et al. 2025, *ApJL*, 995, L53, doi: [10.3847/2041-8213/ae2745](https://doi.org/10.3847/2041-8213/ae2745)

Hascoët, R., Daigne, F., & Mochkovitch, R. 2014, *MNRAS*, 442, 20, doi: [10.1093/mnras/stu750](https://doi.org/10.1093/mnras/stu750)

Huang, Y. F., Dai, Z. G., & Lu, T. 1999, *MNRAS*, 309, 513, doi: [10.1046/j.1365-8711.1999.02887.x](https://doi.org/10.1046/j.1365-8711.1999.02887.x)

Izzo, L., Kuhn, O., Rossi, A., et al. 2024, GRB Coordinates Network, 37925, 1

Izzo, L., Malesani, D. B., Heintz, K. E., et al. 2025, GRB Coordinates Network, 39073, 1

Jin, Z. P., Yan, T., Fan, Y. Z., & Wei, D. M. 2007, *ApJL*, 656, L57, doi: [10.1086/512971](https://doi.org/10.1086/512971)

Khatiya, N. S., Dainotti, M. G., Narendra, A., et al. 2025, *ApJ*, 990, 69, doi: [10.3847/1538-4357/adf219](https://doi.org/10.3847/1538-4357/adf219)

Khokhriakova, A. D., & Popov, S. B. 2019, *Journal of High Energy Astrophysics*, 24, 1, doi: [10.1016/j.jheap.2019.09.004](https://doi.org/10.1016/j.jheap.2019.09.004)

Lan, L., Gao, H., Ai, S., et al. 2025, *ApJS*, 280, 45, doi: [10.3847/1538-4365/adefe4](https://doi.org/10.3847/1538-4365/adefe4)

Lazzati, D., Perna, R., Morsony, B. J., et al. 2018, *PhRvL*, 120, 241103, doi: [10.1103/PhysRevLett.120.241103](https://doi.org/10.1103/PhysRevLett.120.241103)

Li, L., Wu, X.-F., Lei, W.-H., et al. 2018, *ApJS*, 236, 26, doi: [10.3847/1538-4365/aaabf3](https://doi.org/10.3847/1538-4365/aaabf3)

Li, L., Liang, E.-W., Tang, Q.-W., et al. 2012, *ApJ*, 758, 27, doi: [10.1088/0004-637X/758/1/27](https://doi.org/10.1088/0004-637X/758/1/27)

Li, Q.-M., Sun, Q.-B., Qian, S.-B., & Li, F.-X. 2026, *ApJL*, 997, L15, doi: [10.3847/2041-8213/ae2012](https://doi.org/10.3847/2041-8213/ae2012)

Li, R.-Z., Wang, B.-T., Song, F.-F., et al. 2025, GRB Coordinates Network, 38776, 1

Liang, E.-W., Zhang, B.-B., & Zhang, B. 2007, *ApJ*, 670, 565, doi: [10.1086/521870](https://doi.org/10.1086/521870)

Liu, Y., Zhang, Z. B., Dong, X. F., Li, L. B., & Du, X. Y. 2025, *MNRAS*, 542, 215, doi: [10.1093/mnras/staf1217](https://doi.org/10.1093/mnras/staf1217)

Liu, Z.-Y., Zhang, F.-W., & Zhu, S.-Y. 2021, *Research in Astronomy and Astrophysics*, 21, 254, doi: [10.1088/1674-4527/21/10/254](https://doi.org/10.1088/1674-4527/21/10/254)

Lü, H.-J., Zhang, B., Lei, W.-H., Li, Y., & Lasky, P. D. 2015, *ApJ*, 805, 89, doi: [10.1088/0004-637X/805/2/89](https://doi.org/10.1088/0004-637X/805/2/89)

Lynden-Bell, D. 1971, *MNRAS*, 155, 95, doi: [10.1093/mnras/155.1.95](https://doi.org/10.1093/mnras/155.1.95)

Lyons, N., O’Brien, P. T., Zhang, B., et al. 2010, *MNRAS*, 402, 705, doi: [10.1111/j.1365-2966.2009.15538.x](https://doi.org/10.1111/j.1365-2966.2009.15538.x)

Malesani, D. B., Rastinejad, J. C., Levan, A. J., et al. 2025a, GRB Coordinates Network, 38877, 1

Malesani, D. B., Xu, D., Jiang, S. Q., et al. 2023, GRB Coordinates Network, 34485, 1

Malesani, D. B., Cabrera-Lavers, A., Agui Fernandez, J. F., et al. 2024, GRB Coordinates Network, 38080, 1

Malesani, D. B., Saccardi, A., Vergani, S. D., et al. 2025b, GRB Coordinates Network, 38934, 1

Mangano, V., Holland, S. T., Malesani, D., et al. 2007, *A&A*, 470, 105, doi: [10.1051/0004-6361:20077232](https://doi.org/10.1051/0004-6361:20077232)

Margutti, R., Zaninoni, E., Bernardini, M. G., et al. 2013, *MNRAS*, 428, 729, doi: [10.1093/mnras/sts066](https://doi.org/10.1093/mnras/sts066)

Metzger, B. D., Beniamini, P., & Giannios, D. 2018, *ApJ*, 857, 95, doi: [10.3847/1538-4357/aab70c](https://doi.org/10.3847/1538-4357/aab70c)

Moskvitin, A., Pozanenko, A., Moiseev, A., et al. 2023, GRB Coordinates Network, 33187, 1

Moskvitin, A. S., Vinokurov, A. S., Pozanenko, A. S., & GRB follow-up Team. 2024, GRB Coordinates Network, 37916, 1

Perley, D. A., Foley, R. J., Bloom, J. S., & Butler, N. R. 2006, GRB Coordinates Network, 5387, 1

Pescalli, A., Ghirlanda, G., Salvaterra, R., et al. 2016, *A&A*, 587, A40, doi: [10.1051/0004-6361/201526760](https://doi.org/10.1051/0004-6361/201526760)

Planck Collaboration, Ade, P. A. R., Aghanim, N., et al. 2014, *A&A*, 571, A16, doi: [10.1051/0004-6361/201321591](https://doi.org/10.1051/0004-6361/201321591)

Planck Collaboration, Aghanim, N., Akrami, Y., et al. 2020, *A&A*, 641, A6, doi: [10.1051/0004-6361/201833910](https://doi.org/10.1051/0004-6361/201833910)

Ronchini, S., Stratta, G., Rossi, A., et al. 2023, *A&A*, 675, A117, doi: [10.1051/0004-6361/202245348](https://doi.org/10.1051/0004-6361/202245348)

Rossi, E., Lazzati, D., & Rees, M. J. 2002, *MNRAS*, 332, 945, doi: [10.1046/j.1365-8711.2002.05363.x](https://doi.org/10.1046/j.1365-8711.2002.05363.x)

Rowlinson, A., Gompertz, B. P., Dainotti, M., et al. 2014, *MNRAS*, 443, 1779, doi: [10.1093/mnras/stu1277](https://doi.org/10.1093/mnras/stu1277)

Saccardi, A., Malesani, D. B., Corcoran, G., et al. 2025, GRB Coordinates Network, 40228, 1

Salvaterra, R., Della Valle, M., Campana, S., et al. 2009, *Nature*, 461, 1258, doi: [10.1038/nature08445](https://doi.org/10.1038/nature08445)

Sari, R., Piran, T., & Narayan, R. 1998, *ApJL*, 497, L17, doi: [10.1086/311269](https://doi.org/10.1086/311269)

Schneider, B., Malesani, D. B., Fynbo, J. P. U., et al. 2022, GRB Coordinates Network, 32595, 1

Schneider, B., Izzo, L., Saccardi, A., et al. 2024, GRB Coordinates Network, 36176, 1

Schneider, B., Saccardi, A., Malesani, D. B., et al. 2025, GRB Coordinates Network, 39071, 1

Shao, L., Dai, Z. G., & Mirabal, N. 2008, ApJ, 675, 507, doi: [10.1086/527047](https://doi.org/10.1086/527047)

Shen, R., & Matzner, C. D. 2012, ApJ, 744, 36, doi: [10.1088/0004-637X/744/1/36](https://doi.org/10.1088/0004-637X/744/1/36)

Stratta, G., Dainotti, M. G., Dall’Osso, S., Hernandez, X., & De Cesare, G. 2018, ApJ, 869, 155, doi: [10.3847/1538-4357/aadd8f](https://doi.org/10.3847/1538-4357/aadd8f)

Tang, C.-H., Huang, Y.-F., Geng, J.-J., & Zhang, Z.-B. 2019, ApJS, 245, 1, doi: [10.3847/1538-4365/ab4711](https://doi.org/10.3847/1538-4365/ab4711)

Tanvir, N. R., Fox, D. B., Levan, A. J., et al. 2009, Nature, 461, 1254, doi: [10.1038/nature08459](https://doi.org/10.1038/nature08459)

Tian, X., Qin, Y., Du, M., Yi, S.-X., & Tang, Y.-K. 2022, ApJ, 925, 54, doi: [10.3847/1538-4357/ac3de4](https://doi.org/10.3847/1538-4357/ac3de4)

Toma, K., Ioka, K., Yamazaki, R., & Nakamura, T. 2006, ApJL, 640, L139, doi: [10.1086/503384](https://doi.org/10.1086/503384)

Troja, E., Cusumano, G., O’Brien, P. T., et al. 2007, ApJ, 665, 599, doi: [10.1086/519450](https://doi.org/10.1086/519450)

Uhm, Z. L., & Beloborodov, A. M. 2007, ApJL, 665, L93, doi: [10.1086/519837](https://doi.org/10.1086/519837)

Willingale, R., O’Brien, P. T., Osborne, J. P., et al. 2007, ApJ, 662, 1093, doi: [10.1086/517989](https://doi.org/10.1086/517989)

Wu, Q., & EP Collaboration et al. 2025, in prep.

Xu, F., Tang, C.-H., Geng, J.-J., et al. 2021, ApJ, 920, 135, doi: [10.3847/1538-4357/ac158a](https://doi.org/10.3847/1538-4357/ac158a)

Xu, M., & Huang, Y. F. 2012, A&A, 538, A134, doi: [10.1051/0004-6361/201117754](https://doi.org/10.1051/0004-6361/201117754)

Yi, S.-X., Du, M., & Liu, T. 2022, ApJ, 924, 69, doi: [10.3847/1538-4357/ac35e7](https://doi.org/10.3847/1538-4357/ac35e7)

Yi, S.-X., Xi, S.-Q., Yu, H., et al. 2016, ApJS, 224, 20, doi: [10.3847/0067-0049/224/2/20](https://doi.org/10.3847/0067-0049/224/2/20)

Yin, Y.-H. I., Fang, Y., Zhang, B.-B., et al. 2025, ApJL, 989, L39, doi: [10.3847/2041-8213/adf552](https://doi.org/10.3847/2041-8213/adf552)

Yu, H., Wang, F. Y., Dai, Z. G., & Cheng, K. S. 2015a, ApJS, 218, 13, doi: [10.1088/0067-0049/218/1/13](https://doi.org/10.1088/0067-0049/218/1/13)

Yu, Y. B., Wu, X. F., Huang, Y. F., et al. 2015b, MNRAS, 446, 3642, doi: [10.1093/mnras/stu2336](https://doi.org/10.1093/mnras/stu2336)

Zhang, B., Fan, Y. Z., Dyks, J., et al. 2006, ApJ, 642, 354, doi: [10.1086/500723](https://doi.org/10.1086/500723)

Zhang, B., & Mészáros, P. 2001, ApJL, 552, L35, doi: [10.1086/320255](https://doi.org/10.1086/320255)

Zhang, B.-B., Liang, E.-W., & Zhang, B. 2007, ApJ, 666, 1002, doi: [10.1086/519548](https://doi.org/10.1086/519548)

Zhang, G. Q., & Wang, F. Y. 2018, ApJ, 852, 1, doi: [10.3847/1538-4357/aa9ce5](https://doi.org/10.3847/1538-4357/aa9ce5)

Zhao, X.-H. 2025, arXiv e-prints, arXiv:2512.07719. <https://arxiv.org/abs/2512.07719>

Zhu, Z. P., Fu, S. Y., Liu, X., et al. 2025, GRB Coordinates Network, 38759, 1